Single Isolated Pd^{2+} Cations Supported on N-Doped Carbon as Active Sites for Hydrogen Production from Formic Acid Decomposition

Dmitri A. Bulushev,*,[†,‡] Monika Zacharska,[§,⊥] Elena V. Shlyakhova,[‡,#] Andrey L. Chuvilin,[∇,∥]

Yina Guo,[⊥] Sergey Beloshapkin,[⊥] Alexander V. Okotrub,[‡,#] and Lyubov G. Bulusheva*,[‡,#]

[†]Boreskov Institute of Catalysis, SB RAS, 630090 Novosibirsk, Russia

[‡]Novosibirsk State University, 630090 Novosibirsk, Russia

[§]Chemical & Environmental Sciences Department, University of Limerick, Limerick, Ireland

[⊥]Materials & Surface Science Institute, University of Limerick, Limerick, Ireland

[#]Nikolaev Institute of Inorganic Chemistry, SB RAS, 630090 Novosibirsk, Russia

[∇]CIC nanoGUNE Consolider, E-20018 San Sebastian, Spain

[∥]IKERBASQUE, Basque Foundation for Science, Bilbao, Spain

*Correspondence to: dmitri.bulushev@catalysis.ru, bul@niic.nsc.ru

Abstract: Single-site heterogeneous catalysis with isolated Pd atoms was reported earlier mainly for oxidation reactions and for Pd catalysts supported on oxide surfaces. In the present work, we show that single Pd atoms on nitrogen-functionalized mesoporous carbon, observed by aberration-corrected scanning transmission electron microscopy (ac STEM), contribute significantly to the catalytic activity for hydrogen production from vapor-phase formic acid decomposition providing an increase by 2–3 times as compared to Pd catalysts supported on nitrogen-free carbon or unsupported Pd powder. Some gain in selectivity was also achieved. According to X-ray photoelectron spectroscopy (XPS) and near-edge X-ray absorption fine structure (NEXAFS) studies after *ex situ* reduction in hydrogen at 573 K, these species exist in a Pd^{2+} state coordinated by nitrogen species of the support. Extended density functional theory (DFT) calculations confirm that an isolated Pd atom can be the active site for the reaction giving decomposition of formic acid molecule into adsorbed hydrogen atom and carboxyl fragment, but only if it is coordinated by a couple of pyridinic-type nitrogen atoms located on the open edge of graphene sheet. Hence, the role of the N-doping of the carbon support is the formation and stabilization of the new active Pd sites. A long-term experiment performed for more than 30 h on stream indicated an excellent stability of these Pd species in the reaction.

1. INTRODUCTION

Formic acid can be used for hydrogen storage[1,2] or as a hydrogen donor for hydrogen transfer reactions.[3-5] This chemical can be produced with high yields from biomass cellulose via acidic hydrolysis[6] or oxidation.[7] Different metal complexes are widely used as very active homogeneous catalysts for this reaction.[1,2] However, according to our knowledge, only gold species in sub-nm sized state have been reported as active sites for vapor-phase formic acid decomposition. Thus, it was shown[8-11] that these Au species supported on oxide supports are much more active in this reaction than Au nanoparticles. According to Flytzani-Stephanopoulos,[12] the sub-nm species must be assigned to isolated Au-O_x(OH) species attached to the oxide support.

Supported Pd catalysts have very important industrial applications. Normally, the reactions take place over Pd nanoparticles, however, recently the reactivity of single isolated Pd atoms was demonstrated for reactions of oxidation[13-15] and CO_2 reduction.[16] In these studies, Pd was mainly deposited on oxide supports. It should be noticed that while used as a monometallic catalyst, Pd is often supposed to be the best metal to provide high activity and selectivity in hydrogen production from formic acid.[17-20] Pd is also a major constituent of bi- and trimetallic catalysts possessing significantly improved properties for formic acid decomposition as compared to monometallic Pd catalysts.[20,21] The major problem of these catalysts is inhibition of the reaction by CO formed as a by-product in very small concentrations.[17,22]

Carbon materials are widely used as supports for catalysts for different reactions and especially for those related to biomass conversion as these supports are very inert in different media. The chemical composition of the carbon support surface may affect the catalytic properties of supported metals. Thus, we showed that oxidative treatment of carbon spheres support by nitric acid led to deterioration of the performance of the Pd catalyst in formic acid decomposition as compared to the Pd catalyst on the untreated support.[23] However, basing on

our earlier studies of Pt[24] and Ru[25] catalysts on carbon nanofibers, we expect that N-doping would lead to an opposite effect. Nitrogen-doped carbon materials are intensively studied as catalysts and catalysts' supports during last decade. The presence of nitrogen leads to stabilization of a supported phase, changing its chemical and electronic properties or even to creation of novel active sites for catalytic reactions.[24-29]

Recently, Arrigo et al.[27] reported a study of interaction of N-doped carbon nanotubes with Pd species deposited from $Pd(NO_3)_2$ and Na_2PdCl_4 and of reactivity of the obtained catalysts in different reactions like oxygen reduction, CO oxidation and hydrogenation. Our present work is focused to understanding of the nature of Pd species active in decomposition of formic acid and the character of interaction of these Pd species with the N-doped carbon surface. We used novel N-free and N-doped mesoporous carbon materials[30] as catalyst supports and deposited Pd from Pd acetate. This was a chlorine-free and polyvinilpyrrolidone (PVP)-free method providing high dispersion of Pd accompanied by the presence of a considerable content of isolated Pd^{2+} cations stable to the reduction. Using experimental and theoretical approaches, we showed that these isolated Pd species coordinated by pyridinic type nitrogen species of the carbon support are the active sites for the formic acid decomposition reaction.

2. EXPERIMENTAL SECTION

2.1. Materials. Chemicals were purchased from Reachem and Sigma-Aldrich. The iron powder was completely dissolved in acetic acid in an inert atmosphere at 388 K followed by addition of calculated amount of calcium chloride. Then, in order to get iron-doped calcium tartrate, an aqueous solution of sodium tartrate ($Na_2C_4H_4O_6$) was added to the flask containing iron and calcium ions under vigorous stirring. The precipitate was filtered, repeatedly washed with deionized water and dried in air at ambient conditions. According to atomic-absorption

spectral analysis (Hitachi Z-8000, Japan), the concentration of iron in the obtained calcium tartrate was about 0.8 wt.%.

Decomposition of iron-doped calcium tartrate and chemical vapor deposition (CVD) of carbon materials was carried out at 1073 K in a horizontal quartz tube. The reactor chamber was pumped, filled with argon and heated. A certain amount of iron-doped calcium tartrate was uniformly distributed onto ceramic boat, which was placed in the center of the heated reactor by a manipulator. After the decomposition of Ca tartrate during 10 min under dynamic vacuum, ethanol or acetonitrile vapor was fed for 30 min. The resultant product was immersed into dilute HCl acid to remove calcium and iron containing species, subsequently washed with distilled water and dried in air at 373 K overnight. The materials obtained from ethanol and acetonitrile were denoted as C_M and N-C_M, respectively.

Pd was deposited on these carbon supports using incipient wetness impregnation. For this, Pd acetate was mixed with acetone or water in an amount to provide the metal content of 1 wt. %. After the complete consumption of the solution by the support, the materials were dried overnight at 353 K in air and were reduced in hydrogen before the catalytic experiments as it is described below.

2.2. Characterization. An elemental analyzer (EuroVector EA3000, Italy) equipped with a thermal conductivity detector (TCD) was used to determine the carbon, hydrogen and nitrogen (CHN) contents in the N-C_M sample. The sample was placed in a separate tin foil vial and then combusted completely in a high purity oxygen environment at 1273 K. Helium was used as a carrier gas. The obtained gases were then separated in a gas chromatography column and quantified. The instrument was calibrated using a high purity acetanilide standard.

Nitrogen adsorption-desorption isotherms were obtained using an Autosorb–iQ (Quantachrome Instruments, USA) at 77 K. Before the measurements, the samples were degassed at 473 K for 12 h under dynamic vacuum. The total surface area was calculated from adsorption data using the Brunauer-Emmett-Teller (BET) equation. The total pore volume was

obtained from the uptake of nitrogen at $P/P_0=0.95$ and the pore size distribution was determined by the Barret-Joyner-Halenda (BJH) method.

X-ray photoelectron spectroscopy (XPS) and near-edge X-ray absorption fine structure (NEXAFS) spectra were recorded at the Berliner Elektronen-speicherring für Synchrotronstrahlung (BESSY) using radiation from the Russian-German beamline. The overall XPS spectra were measured at the energy of monochromatized synchrotron radiation of 800 eV with a resolution of 0.5 eV full width at half maximum (FWHM). NEXAFS spectra near the CK- and NK-edges were acquired in the total-electron yield mode. As compared to the conventional XPS measurements, these measurements provided a lower depth of sample analysis. The spectra were normalized to the primary photon current from a gold-covered grid recorded simultaneously. The monochromatization of the incident radiation was ~80 meV for the carbon region and ~170 meV for the nitrogen region (FWHM). It is known that metallic Pd is covered by a thin oxide layer in ambient air. To remove the species, which can be formed on the Pd surface during storage in laboratory conditions, we performed an *ex situ* reduction. For this, the Pd catalysts already reduced in a catalytic reactor were heated in H_2 (about 2.3 Pa) in a preparation chamber of the spectrometer at 613 K for 3.5 h. After cooling to room temperature, the samples were transferred to a measurement chamber in ultra-high vacuum conditions (10^{-6} Pa).

In addition, XPS measurements of Pd states were performed on a conventional AXIS Ultra DLD spectrometer (Kratos, UK) using monochromatic Al Kα radiation (1486.6 eV). The C 1s line at 284.8 eV was taken for reference energy calibration. An *ex situ* reduction of the samples for these measurements was performed in 33 Pa of hydrogen at 573 K for 30 min in the preparation chamber of the XPS unit.

The morphology of the samples was studied using a Titan 60-300 TEM/STEM image-side Cs-corrected microscope (FEI, Netherlands) at acceleration voltage of 80 kV for TEM and 300 kV for scanning TEM (STEM). The samples in this case were prepared by ultrasound-assisted

deposition of isopropanol suspension of the material on lacey carbon film grids. Pd particle size distributions were obtained using a regular JEM-2100F microscope (JEOL, Japan) with an acceleration voltage of 200 kV in STEM mode with a high-angle annular dark-field (HAADF) detector.

2.3. Catalytic experiments. Vapor-phase formic acid decomposition was carried out in a fixed bed tubular quartz reactor with 4 mm internal diameter as was described earlier.[17,25] Activity tests were performed at atmospheric pressure with 7 mg of catalyst placed between two layers of quartz wool. The catalysts were reduced in an 1 vol.% H_2/Ar mixture at 573 K for 1 h and cooled in He to the reaction temperature (333 K). To obtain a temperature dependence of the acid conversion, the composition of the outlet gas mixture was measured several times at each temperature (at least for 30 min) to ensure that steady-state was reached. Two such cycles have been performed to stabilize the catalyst before obtaining the conversion-temperature dependences shown in that paper.

The reaction mixture contained 1.9 vol.% of formic acid in He. All experiments were performed with a total flow rate of 51 cm^3 (STP) min^{-1}. The reactants and products were analyzed by a gas chromatograph (HP-5890) fitted with a Porapak-Q column and a thermal conductivity detector.

As no other carbon containing products were detected, the conversion of formic acid was determined as a sum of the concentrations of CO and CO_2 formed related to the initial concentration of formic acid. Turnover frequencies (TOF) were calculated at conversions lower than 20%. The TOF values were determined as the sum of the rates of the formation of CO and CO_2 molecules related to the total number of Pd atoms in the samples.

2.4. Computational details. Theoretical modeling was carried out using a gradient-corrected functional of Perdew-Burke-Ernzerhof (PBE) with local and nonlocal exchange and correlation[31] within the quantum-chemical program package Jaguar (Jaguar, version 7.9, Schrödinger, LLC, New York, NY, 2012). Atomic orbitals were described by a LACVP basis set, where the

outermost core orbitals were included for Pd and the 6-31G set was applied for light elements. An N-doped carbon substrate was modeled by a nitrogen-containing graphene fragment with hydrogen-terminated edges. The geometry of the models with a Pd atom located at different sites of the fragment was optimized by an analytical gradient method until the energy was converged to be better than $5 \cdot 10^{-5}$ Hartree/Bohr. Binding energy of the Pd atom to graphene fragment was calculated as: $E^{bind} = E^{tot}(\text{fragment}) + E^{tot}(\text{Pd}) - E^{tot}(\text{model})$, where E^x is a total energy of the isolated initial N-doped graphene fragment, the single Pd atom, and the model, respectively. For calculation of the interaction of Pd-containing models with formic acid, we used LACVP*+ basis set with polarization functions placed on carbon, nitrogen and oxygen atoms and diffuse functions used for all atoms except of hydrogen. Binding energy of formic acid (FA) in those models was calculated as: $E^{bind} = E^{tot}(\text{Pd-fragment}) + E^{tot}(\text{FA}) - E^{tot}(\text{model})$, where E^x is a total energy of the isolated N-doped graphene fragment with anchored Pd, free formic acid molecule, and the model, respectively.

3. RESULTS AND DISCUSSION

3.1. Characterization of carbon supports and Pd catalysts. A study of the chemical composition of the N-doped carbon support showed the presence of carbon, nitrogen, hydrogen and oxygen (Table S1, Supporting information). The presence of calcium and iron was not found by XPS indicating that the purification of the materials in HCl was efficient. The N-free sample did not contain any nitrogen, but the content of oxygen was quite similar to that in the N-doped sample (6-7 at.%). The bulk content of nitrogen in the N-doped sample corresponded to 5.9 wt.% or 4.7 at.%. This sample contained also about 11 at.% of hydrogen. The bulk and surface compositions were quite similar indicating that the elements are distributed uniformly throughout the material.

Textural characteristics of the obtained carbon materials were determined from nitrogen sorption measurements. The adsorption/desorption isotherms for both materials could be assigned to type II (Figure S1a, Supporting information) reflecting a mesoporous nature of the samples. Based on the sorption isotherms, specific surface area, pore volume and pore size distributions were determined and summarized in Table 1. The N-C_M and C_M samples showed BET specific surface areas of 671 and 414 m^2 g^{-1} and pore volumes of 1.40 and 0.89 cm^3 g^{-1},

Table 1. Textural properties of the used carbon supports

Sample	S_{BET}, m^2 g^{-1}	Specific pore volume, cm^3 g^{-1}	Average pore diameter, nm
C_M	414	0.89	13
N-C_M	671	1.40	13

respectively. An intensive peak appeared in the pore size distributions (Figure S1b, Supporting information) at 13 nm for the both samples indicating the presence of relatively uniform size mesopores.

Palladium was deposited from Pd acetate mixed with water or acetone. It is known that Pd acetate is badly dissolved in water, but nicely in acetone. Earlier, Kondrat et al.[32] showed that there is even no need to use any solvent for Pd acetate deposition as nanoparticles of Pd (2–4 nm) can be formed in a grinded mixture of Pd acetate with activated carbon at temperatures higher than 453 K in inert atmosphere. However, such dry method of preparation also gave some big Pd particles of ~20 nm in size, which were not observed in our study.

The presence of mesopores is also clearly seen in the HAADF/STEM images of the samples with deposited Pd (Figure S2, Supporting information). This was in agreement with the textural studies of the samples (Table 1). The morphologies of the samples with and without
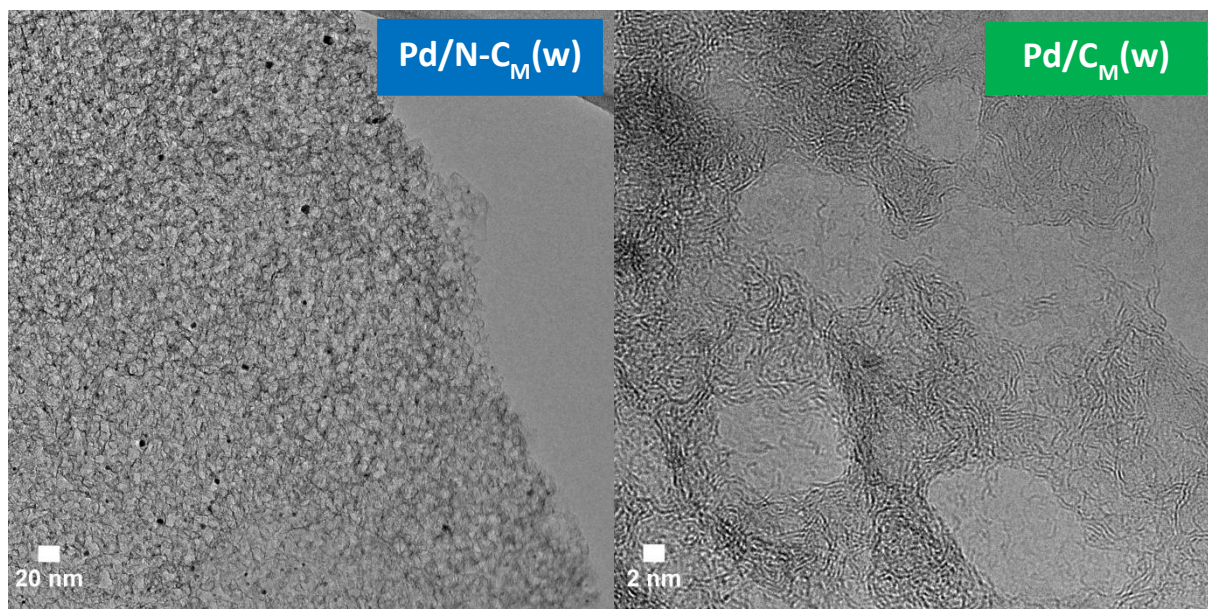

Figure 1. TEM images of the reduced Pd catalysts (Titan 60-300).

nitrogen are similar and remind a sponge. TEM images taken at a higher magnification (Figure 1) showed that the structure of the supports is created by disordered few-layer graphene-like flakes. The presence of multiple open edge sites is observed. Concluding, the morphology of the samples is determined mainly by the catalyst used for the growth of the carbon material and not by the carbon precursor used. The pore structure is created by CaO_x nanoparticles produced under thermolysis of Ca tartrate used for synthesis of the support.[30]

Mean Pd particle sizes and particle size distributions were determined for the catalysts using HAADF/STEM images obtained by regular TEM (Figure 2, Table 2). It is seen that if Pd acetate is deposited from the same solvent (water) on the N-free and N-doped carbon samples, the mean particle size for the N-free catalyst is 2.5 nm, while that for the N-doped sample is bigger (3.4 nm). To elucidate the effect of nitrogen, the comparison of the catalytic activity has
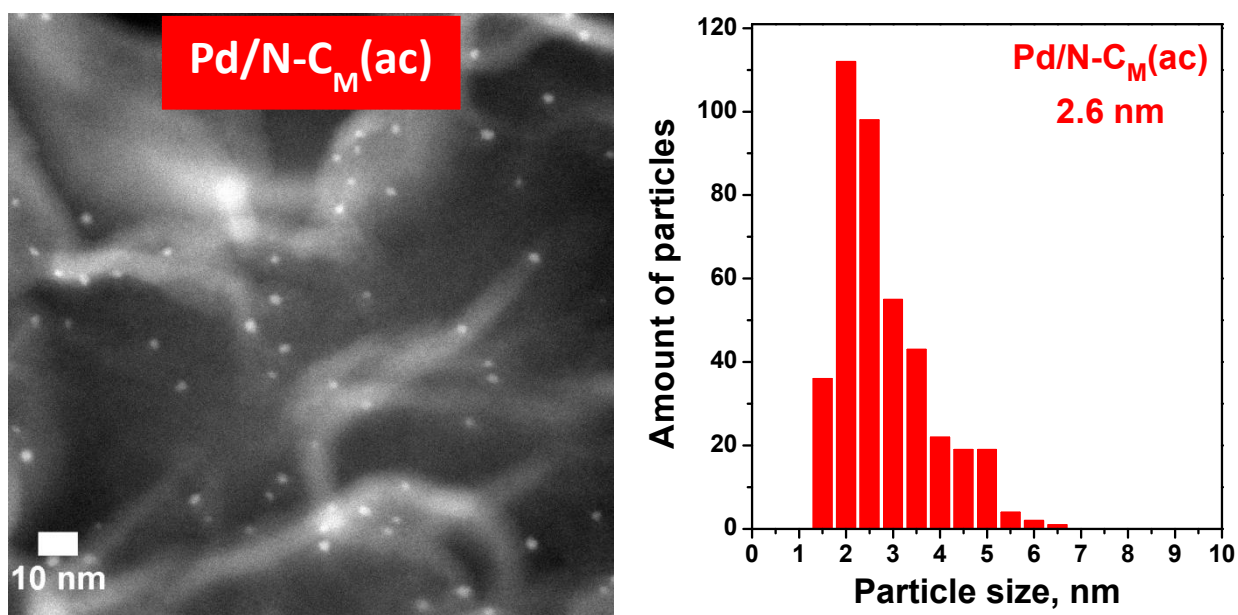
11
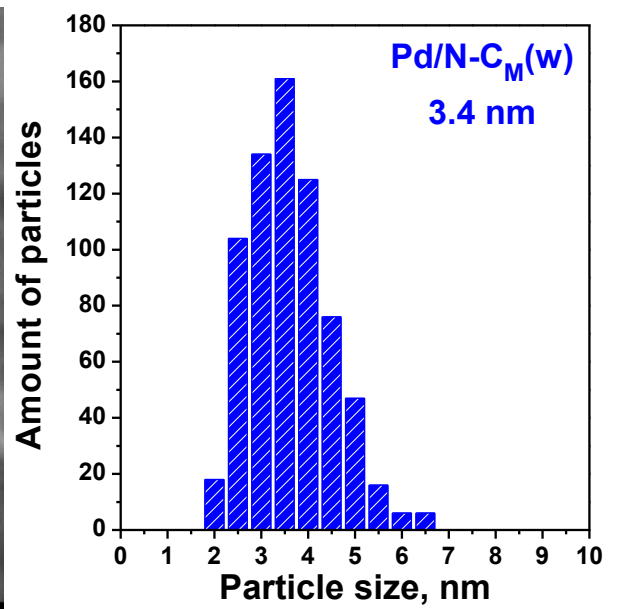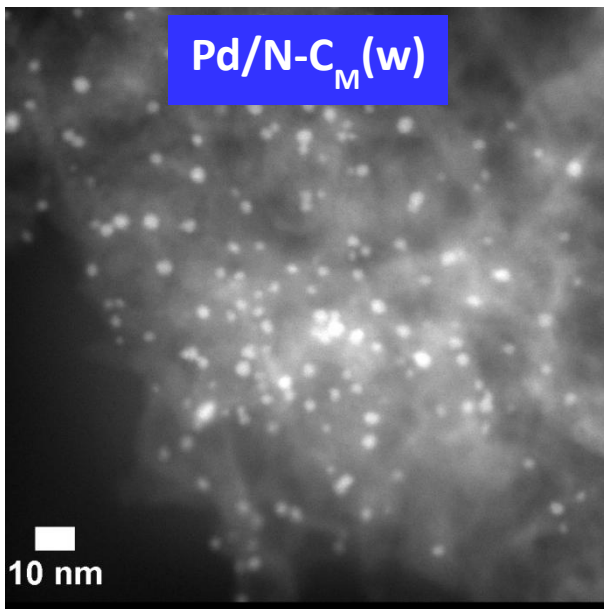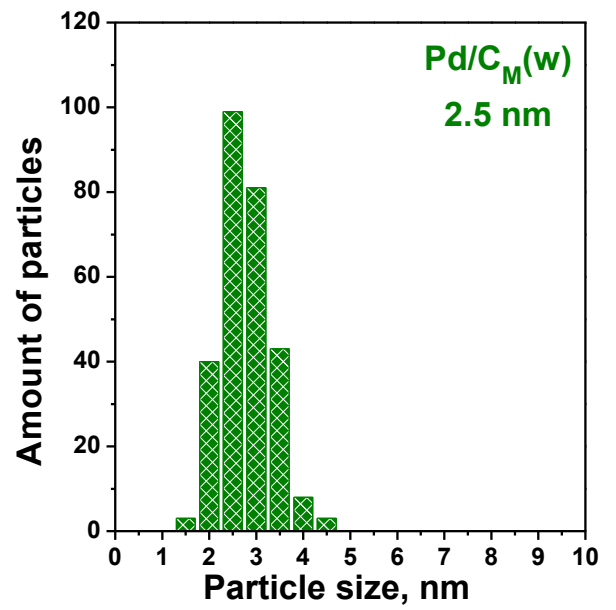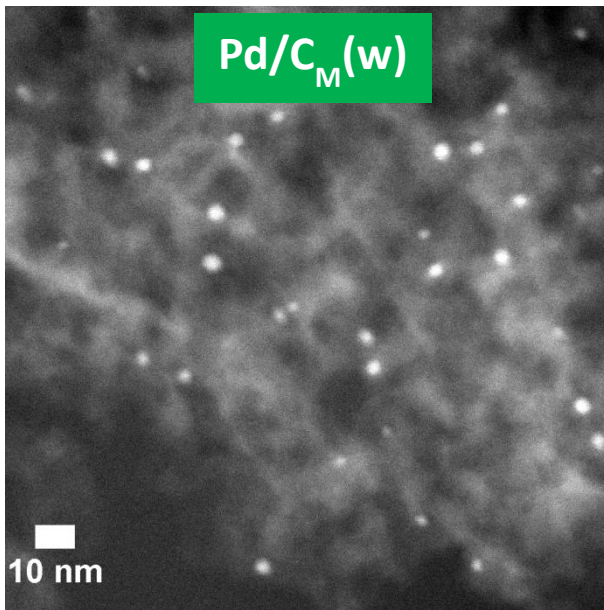
Figure 2. HAADF/STEM images and Pd particle size distributions for the Pd catalysts after reduction/reaction (JEM-2100F).

Table 2. Mean Pd particle size determined by HAADF/STEM (JEM-2100F) and catalytic data

Catalyst	Mean particle size, nm	TOF at 373 K, s^{-1}	Temperature of 50% conversion, K	Hydrogen selectivity at 50% conversion, %
Pd/C_M(w)	2.5 ± 0.5	0.034	444	93.7
Pd/N-C_M(ac)	2.6 ± 1.0	0.121	422	95.5

12

Pd/N-C$_M$(w)	3.4 ± 0.9	0.07	436	94.8
Pd/C[17,18] (Sigma-Aldrich)	3.6 ± 1.7	0.022	-	-
Unsupported Pd powder[33] (Alfa Aesar)	25[a]	0.039[b]	-	-

[a] determined from BET surface measurements

[b] determined per surface Pd atom

to be done with the catalysts having the same mean particle size to avoid particle size effects, which can mask the effect of nitrogen incorporated into the support. Hence, acetone was used instead of water to disperse Pd acetate to get a smaller mean particle size (2.6 nm) for the N-doped catalyst similar to that for the N-free sample (2.5 nm). Figure 2 and Table 2 show also that the particle size distributions are slightly broader for the N-doped catalysts as compared to the N-free sample. The effect of solvent on the mean particle size is probably related to partial hydrolysis of Pd acetate in water giving Pd oxo-/hydroxospecies as precursors for Pd clusters in contrast to the case of the Pd acetate precursor in acetone.

3.2. Catalytic reaction. The catalysts as well as catalysts supports were tested in the formic acid decomposition reaction and the data are shown in Figure 3 and Table 2. It is seen that the activity of the supports was negligible as compared to the activity of the Pd catalysts. The N-doping provided a shift of the temperature of 50% conversion (T$_{50}$) by 22 K to lower

values. When comparing the activities of the Pd catalysts at low temperatures (<400 K), the conversions of formic acid (Figure 3) and TOF values (Table 2) for the N-doped catalysts were 2-3 times higher than that for the N-free catalyst. It is also important that the TOF values for the N-doped samples were higher than those for the unsupported Pd powder[33] and commercial 1 wt.% Pd/C catalyst[17,18] with a mean particle size of 3.6 nm close to that for the Pd/N-C_M(w) sample. Both the Pd powder and Pd/C sample were studied by us earlier at the same reaction
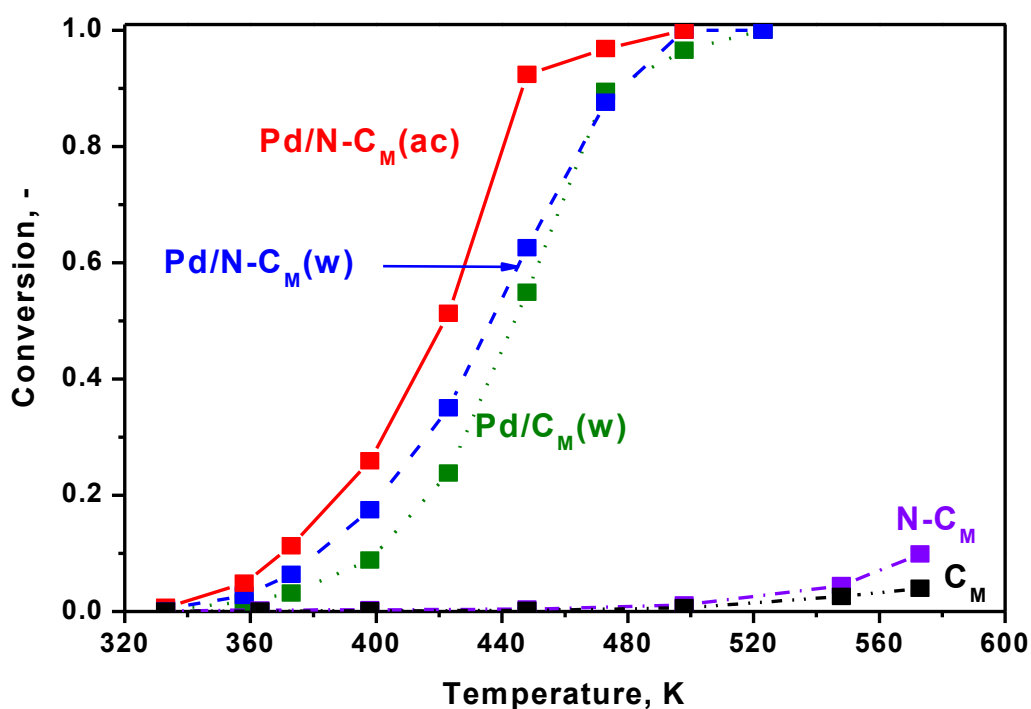

Figure 3. Temperature dependences of the formic acid conversion over catalyst supports and Pd catalysts prepared from Pd acetate in water (w) or acetone (ac) solutions.

conditions. The selectivity of hydrogen production also increased with N-doping, from 93.7 to 95.5% indicating that the content of CO in the reaction products decreased by 1.5 times. Generally, similar effects of N-doping of carbon for the formic acid decomposition we observed

for highly dispersed Ru[25] and Pt[24] catalysts supported on another type of carbon - carbon nanofibers.

A stability test was performed with the Pd/N-C$_M$(ac) sample (Figure 4). In this experiment formic acid was introduced into the dried, but unreduced sample, at 448 K for 35 h, then the reduction was performed in H$_2$ at 573 K for 1 h as normally and then after cooling back to 448 K in He, the gas flow containing formic acid was introduced again for 30 h. It is seen that the reduction is not necessary to get the same steady-state activity as after the reduction the same steady-state state of the catalyst is formed in the conditions of the formic acid decomposition reaction. However, the initial transient period was relatively long (1 h). This indicates that the necessary decomposition of the existing at the beginning of the run Pd acetate liberating the active Pd sites is slow at this temperature. This is in accordance with the data of Kondrat et al.[32] who observed by the thermal gravimetric method that the decomposition of Pd acetate in inert
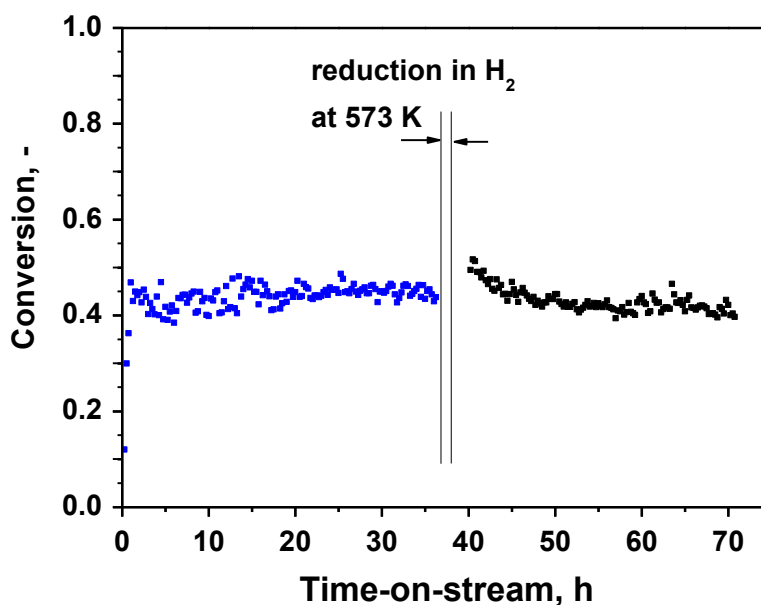

Figure 4. Dependence of the conversion of formic acid over the Pd/N-C$_M$(ac) sample on time-on-stream at 448 K.

gas starts only at about 453 K.[32] The experiment presented in Figure 4 also clearly showed that the active sites are very stable in the conditions of the formic acid decomposition reaction as there was no deactivation observed.

Therefore, the Pd catalyst on the N-doped support prepared from acetone solution provided the catalytic activity, which is 3 times higher than that of the N-free catalyst (Figure 3, Table 2). The particle size distributions for these two samples are shown in Figure 2 and are also compared on the same plot (Figure S3, Supporting information). The comparison indicates that both Pd catalysts possess the same mean particle size and the difference in the particle size distributions is very small and can hardly explain the difference in the catalytic activity. Hence, the N-doping effect cannot be related to the difference in the particle sizes observed by regular TEM. We also did not find a difference in the shape of the metal nanoparticles on the N-doped and N-free carbon supports. Hence, aberration-corrected STEM allowing discrimination of atoms and clusters with a few atoms was applied in order to understand whether there are some smaller Pd clusters or even isolated atoms in the samples than those seen by regular TEM (Figure 2). These smaller Pd species must be more sensitive to the presence of nitrogen in the vicinity than Pd nanoparticles and this could influence significantly their catalytic properties.

3.3. Pd interaction with the support. Figure 5 and Figure S4 (Supporting information) show HAADF/STEM images of the Pd/N-C$_M$ sample taken with a Titan 60-300 microscope. It is seen that except of the presence of Pd clusters of 1–2 nm observed as big bright white spots the image demonstrates the presence of much smaller species: isolated atoms and clusters with a few atoms. They are seen as light-gray dots distributed uniformly through the carbon matrix. These species cannot be assigned to nitrogen species as they are not discriminated from carbon by this equipment, because of close Z-contrast. Hence, they must be assigned to Pd species. Moreover, as the typical size of the light-gray dot is about 2-3 Å, they should be assigned mainly to single
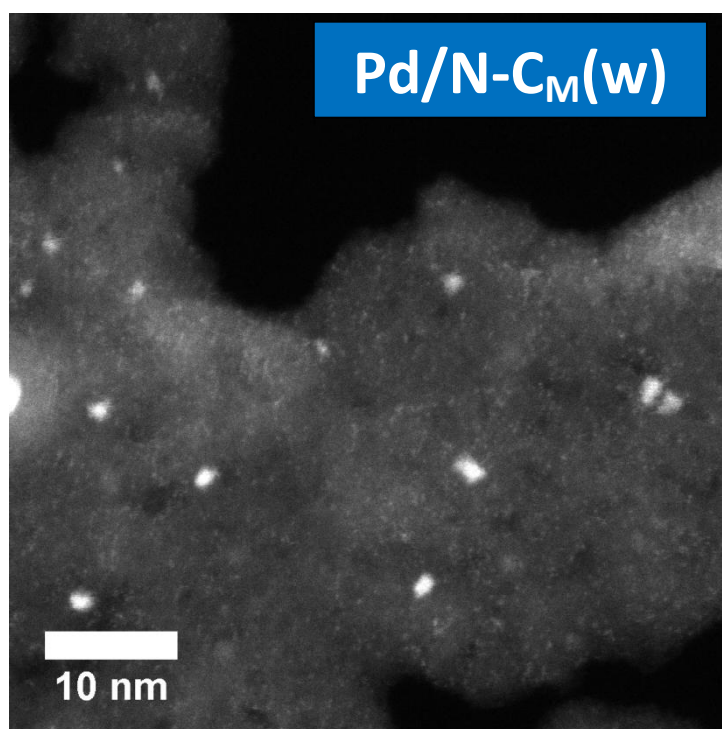
Figure 5. HAADF/STEM image with atomic resolution of the reduced Pd/N-C_M(w) catalyst (Titan 60-300).
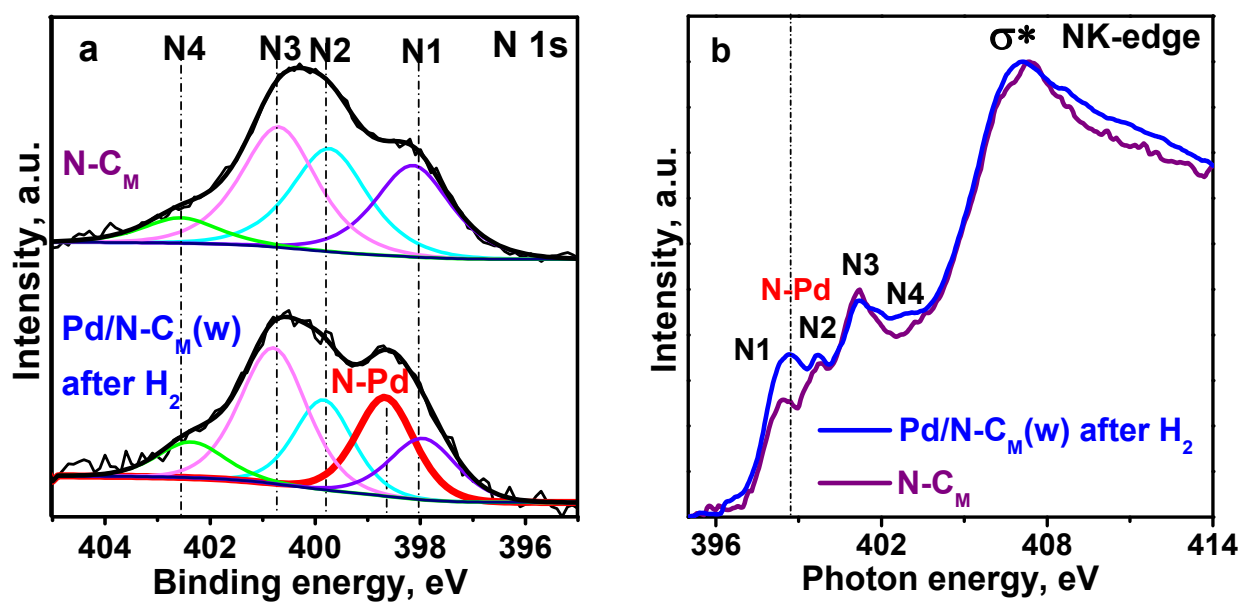

Figure 6. (a) XPS N 1s spectra and (b) NEXAFS NK-edge spectra for the N-C_M support and Pd/N-C_M(w) catalyst reduced *ex situ*.

atoms/cations. This observation gives a good reason to suppose that the single isolated Pd atoms could be the active sites for the reaction if they are coordinated by nitrogen species of the support providing the observed promotion of the catalytic activity (Figure 3, Table 2).

The state of nitrogen and Pd in the samples was studied using XPS and NEXAFS. Figure 6a shows XPS N 1s spectra of the carbon support without Pd corresponding to different nitrogen species revealing that nitrogen is imbedded into the carbon structure in four forms. The N 1s lines at ~398.1 (N1), ~399.8 (N2), ~400.7 (N3) and ~402.4 eV (N4) were attributed to pyridinic, pyrrolic, graphitic and oxidized nitrogen species, respectively.[25,27,34,35] The first three species are present in approximately the same concentrations (~30%, Table S2, Supporting information). For the samples with the reduced deposited Pd, a better fit of the N 1s spectra could be achieved accepting the presence of one more type of nitrogen species with a binding energy of 398.7–398.8 eV. We have assigned it to nitrogen species interacting with Pd (N-Pd component). This line is in agreement with the recent results of Arrigo et al.[28] showing a significant increase of the peak in the same region after deposition of PdAu nanoparticles on N-functionalized carbon nanotubes.

The NEXAFS study confirmed the change in the chemical state of nitrogen in the N-C_M material after the Pd deposition/reduction (Figure 6b). To visualize this more clearly, the NK-edge spectra were normalized to the intensity of the σ* resonance. The spectrum of the initial N-C_M support showed three peaks located at ~398.4, ~399.8, and ~401.2 eV attributed to pyridinic, pyrrolic and graphitic forms of nitrogen, respectively, in accordance with the XPS data. The oxidized nitrogen species (N4) could be responsible for a shoulder at the high-energy side of the peak. It is seen in Figure 6b that the Pd deposition/reduction leads to a change of the states of nitrogen in the sample. The NK-edge spectra of the Pd/N-C_M sample exhibited an increase of the intensity between the low-energy peaks N1 and N2 similarly to the XPS result (Figure 6a). A new peak at ~398.9 eV, which was absent for the N-C_M support, has to be assigned to the

nitrogen species interacting with Pd. Hence, it would be important to discover a difference related to the appearance of the N-Pd interaction also in the XPS spectra of Pd.

It must be pointed out that before the measurements of the Pd spectra by XPS the oxide layer covering Pd surface formed because of the contact of the sample with air must be removed as its presence masks the effect of nitrogen. The presence of such layer accompanied by the appearance of lines assigned to Pd^{2+} cations is seen in the XPS spectra of the original unsupported Pd powder (Figure 7a) obtained with the conventional equipment. The layer was completely removed after the reduction *ex situ* performed according the procedure described in Experimental Section. The XPS measurements of the Pd electronic state in the *ex situ* reduced supported samples are shown in Figure 7b. The Pd 3d spectrum consisted of 2 doublets with $3d_{5/2}$ positions at about 335.9 and about 338.0 eV typical for supported Pd metallic clusters and ionic Pd^{2+} species,[27] respectively. So, in contrast to the unsupported Pd powder, the Pd^{2+} species were present in a significant concentration in the N-free and N-doped samples in spite of the
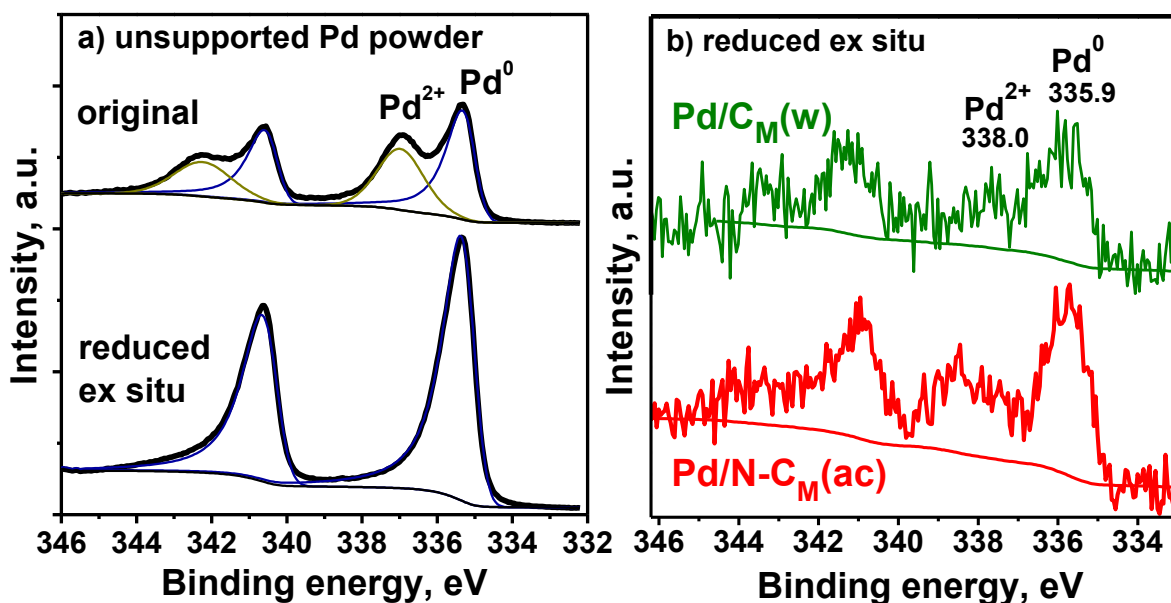

Figure 7. Pd 3d XPS spectra of the (a) original and reduced *ex situ* unsupported Pd powder and (b) supported Pd samples reduced *ex situ*.

performed reduction. The content of the Pd^{2+} species was higher in the N-doped sample as compared to the N-free one in accordance with the XPS data. The positions of the Pd 3d peaks corresponding to metallic Pd (Pd^0) do not change noticeably with nitrogen doping of the support indicating that the electronic properties of Pd nanoparticles do not change.

As the unsupported Pd powder does not show the presence of the Pd^{2+} species after the same reduction (Figure 7a), the presence of this oxidized Pd form in the supported catalysts was assigned to highly dispersed Pd species strongly interacting with the support through oxygen or nitrogen atoms. The higher content of the Pd^{2+} species on the N-doped support indicates that part of these species is stabilized by nitrogen atoms of the support like in some metal complexes. These Pd^{2+} species could be related to the isolated Pd atoms observed by aberration-corrected STEM (Figure 5 and Figure S4, Supporting information). Hence, the atoms seen by aberration-corrected STEM are in the Pd^{2+} state stabilized by nitrogen of the support. Very recently, Arrigo et al.[27] observed similar changes in NEXAFS spectra of nitrogen after Pd deposition and assigned them to the formation of a covalent bond of Pd with pyridinic nitrogen with partial ionic character consistent with the shift of the binding energy of Pd 3d close to the Pd^{2+} state. Earlier, we reported a strong shift of the Pt 4f binding energy for 100% dispersed Pt deposited on N-doped carbon nanofibers as compared to 100% dispersed Pt deposited on N-free carbon nanofibers.[24] Arrigo et al.[27] also noticed that coordination of Pd^{2+} species to nitrogen of the support complicates the reduction of these species with hydrogen. Stonkus et al.[29] confirmed that deposition of Pd on N-doped carbon nanofibers leads to a change of redox properties of Pd as compared to those for Pd supported on N-free carbon nanofibers.

3.4. Preferable sites for Pd anchoring. To check the preferable sites for the attachment of a Pd atom in the $N-C_M$ sample we invoked DFT calculations of models. Though four different nitrogen forms were identified in $N-C_M$ sample, we excluded the oxidized N species from the consideration as their amount was low. Thereby, graphitic (Ngr), pyrrolic (NH), and pyridinic

(Nv, Ne) nitrogen atoms were introduced into a graphene fragment (Figure 8). Pyridinic or two-fold coordinated nitrogen atom may have various local surroundings, particularly; it can be located at the boundary of a vacancy or at the edge of graphene sheet. In our case, a single pyridinic nitrogen atom was positioned at the monovacancy boundary (Nv) and two pyridinic nitrogen atoms substituted carbon atoms at the armchair edge (Ne). The absolute values of Kohn-Sham N 1s energies for these atoms are presented in Table S3 (Supporting information) together with the binding energies of corresponding nitrogen species derived from the fitting of the XPS N 1s spectra of the N-C_M and Pd/N-C_M samples (Figure 6a). The difference between the values is due to the calculation of the ground state of the N-doped graphene fragment, while XPS probes the excited state. Nonetheless, the theory gives a correct sequence of the N 1s energies as N(graphitic) > N(pyrrolic) > N(pyridinic). These results are in line with the DFT calculations performed earlier by Artyushkova et al.[35]

A Pd atom was placed into one of the numbered sites in the graphene fragment (Figure 8): (1) between two edged pyridinic nitrogen atoms (Ne), (2) graphitic nitrogen (Ngr) or (3) pyridinic nitrogen (Nv), (4) above the C–C bond near the pentagon, (5) Nv atom, (6) Ngr atoms and (7,8) far from any nitrogen defect. Further, the obtained models (Figure S5, Supporting
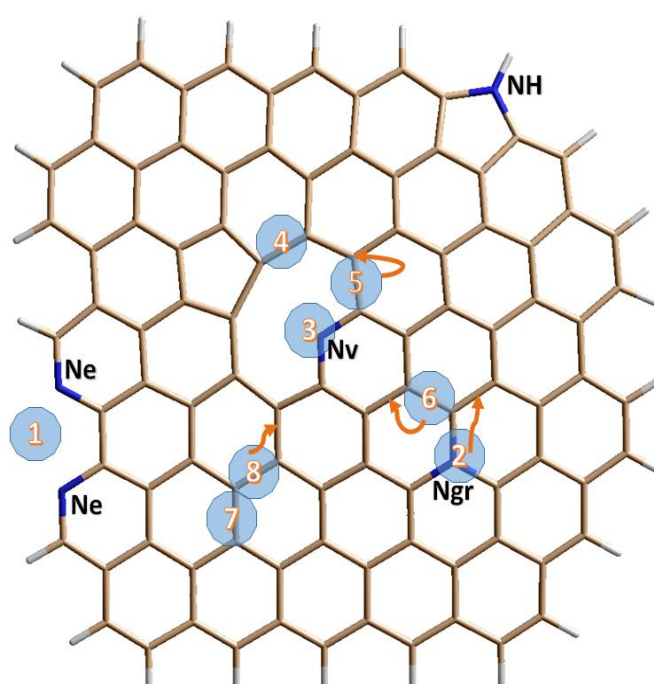
Figure 8. Optimized geometry of graphene fragment containing various nitrogen species: Ngr – graphitic nitrogen, Nv – pyridinic nitrogen at a vacancy, Ne – pyridinic nitrogen at graphene edge, NH – pyrrolic nitrogen. The numbers in the circles show the sites for initial placement of Pd atoms; the arrows show direction of moving of Pd atoms (if any) as the result of relaxation of geometry of the model.

Table 3. Binding energy for a Pd atom anchored to different sites of nitrogen-containing graphene fragment (models 1–8 in Figure 8 and Figure S5 (Supporting information))

model	1	2	3	4	5	6	7	8
E^{bind} (eV)	2.21	1.15	1.20	1.68	1.30	1.22	1.11	1.19

information) will be referred in correspondence with these numbers. The calculated binding energies of Pd atoms in the models are collected in Table 3. Relaxations of the geometry of the models revealed that the Pd atom readily interacts with pyridinic nitrogen atoms (sites 1 and 3). The highest binding energy was obtained for the model 1, where the Pd atom is attached to two pyridinic nitrogen atoms at the graphene fragment edge. The similar energy values were found in calculations of interaction of a Pd atom with three pyridinic nitrogen atoms or a pair of the atoms surrounding a monovacancy in a carbon nanotube.[36,37] The Pd atom, which was located above the Ngr site in the starting configuration (site 2), moved to the neighboring carbon sites and formed a bridge above the C–C bond in accordance with calculations performed by Li et al.[38] for adsorption of a Pt atom on a carbon nanotube containing graphitic nitrogen. We observed changes in the location of the Pd atom for the starting sites 6 and 8. In the former case, the atom occupied the position between Nv and Ngr atoms after optimization of geometry. In the latter

case, the Pd atom moved to the vacancy. Tang et al.[39] also obtained a higher binding energy of a Pd atom with a defect site (monovacancy) in graphene as compared to that for perfect graphene.

Analyzing the results of the calculations, we conclude that a Pd atom is quite mobile on a graphene sheet and it likes to be close to defect sites such as vacancies (models 4, 5, 8) or incorporated nitrogen atoms (models 1, 6, 3). The Pd atom prefers to form a bridge with two carbon atoms located above the center of the C–C bond. As concerning to bonding with nitrogen species, Pd does not bind with graphitic nitrogen, whereas readily interacts with pyridinic nitrogen. Our calculations predict an increase of the N 1s binding energy of the pyridinic nitrogen after its binding with a Pd atom (Table S3, Supporting information) that agrees well with the experimental XPS and NEXAFS observations. This shift is explained by the influence of delocalized π-electron system of graphene network on electron density redistribution. The powerful electron cloud pulls the density from the interacting atoms: pyridinic nitrogen and Pd atom. To confirm this effect for our system, we calculated the electron density surfaces for N-containing graphene fragments before and after the attachment of the Pd atom (Figure S6, Supporting information). Covalent bonding of a Pd atom with two pyridinic N atoms causes more positive charging of N atoms relatively to the initial states. Although the core electrons of N and Pd do not participate in the bonding, they feel the change in the electrostatic potential. And the increase of the potential on N atoms as the result of the Pd attachment results in an increase of the binding energy of the N 1s electrons, which we detected for eigenvalues of N 1s levels in the model 1 and observed experimentally in the XPS N 1s spectrum.

3.5. Interaction of formic acid with anchored Pd. To support the experimental data determined a several times higher catalytic activity of the Pd/N-C_M system as compared to the Pd/C_M one, we performed a calculation of interaction of formic acid molecule with structures presented in the models 1, 4, 5, 6 and 7 (Figure 8 and Figure S5, Supporting information). The model 1, where a Pd atom interacts with two edged pyridinic nitrogen atoms, is the most

energetically favorable in the considered set of models. The model 4, where the Pd atom is at the monovacancy boundary, is the next in the stability trend. The models 5 and 6 were chosen to reveal a promoting effect of pyridinic nitrogen located in the vicinity of the carbon-bonded Pd atom. Finally, the model 7 simulates the N-free Pd/C_M system.

The relaxed structures and binding energies of the formic acid molecule to the Pd atom anchored to a certain site of nitrogen-containing graphitic fragment are demonstrated in Figure 9. The molecule interacts most strongly with Pd in the model 1. The weakest bonding is with the N-free graphene region (model 7). Interactions of formic acid with Pd in the models 4 and 5 give the same energy gain. In these models, the Pd atom is located at the center of the C–C bond, which is close to the monovacancy with a nitrogen atom at the boundary. The interaction with the model 6 is the next in the energy gain after the model 1. In this structure, the Pd atom is between pyridinic and graphitic nitrogen species. We conclude that although graphitic nitrogen does not interact directly with Pd, this nitrogen species influences the electronic state of the anchoring Pd atom thus increasing the strength of the interaction with formic acid. A pyridinic nitrogen atom located at the monovacancy boundary provides an additional stabilization of the formic acid molecule through the N–H bonding (see bond lengths in Table S4, Supporting information). As a result, the Pd atom deviates slightly toward the pyridinic nitrogen (Figure 9). Finally, the calculations show that formic acid prefers interacting with a Pd atom via C and/or H of the –CH group.

Now, we focus a special attention on the model 1, because it was a sole case, when the formic acid molecule was decomposed as the result of interaction with a Pd atom. In the
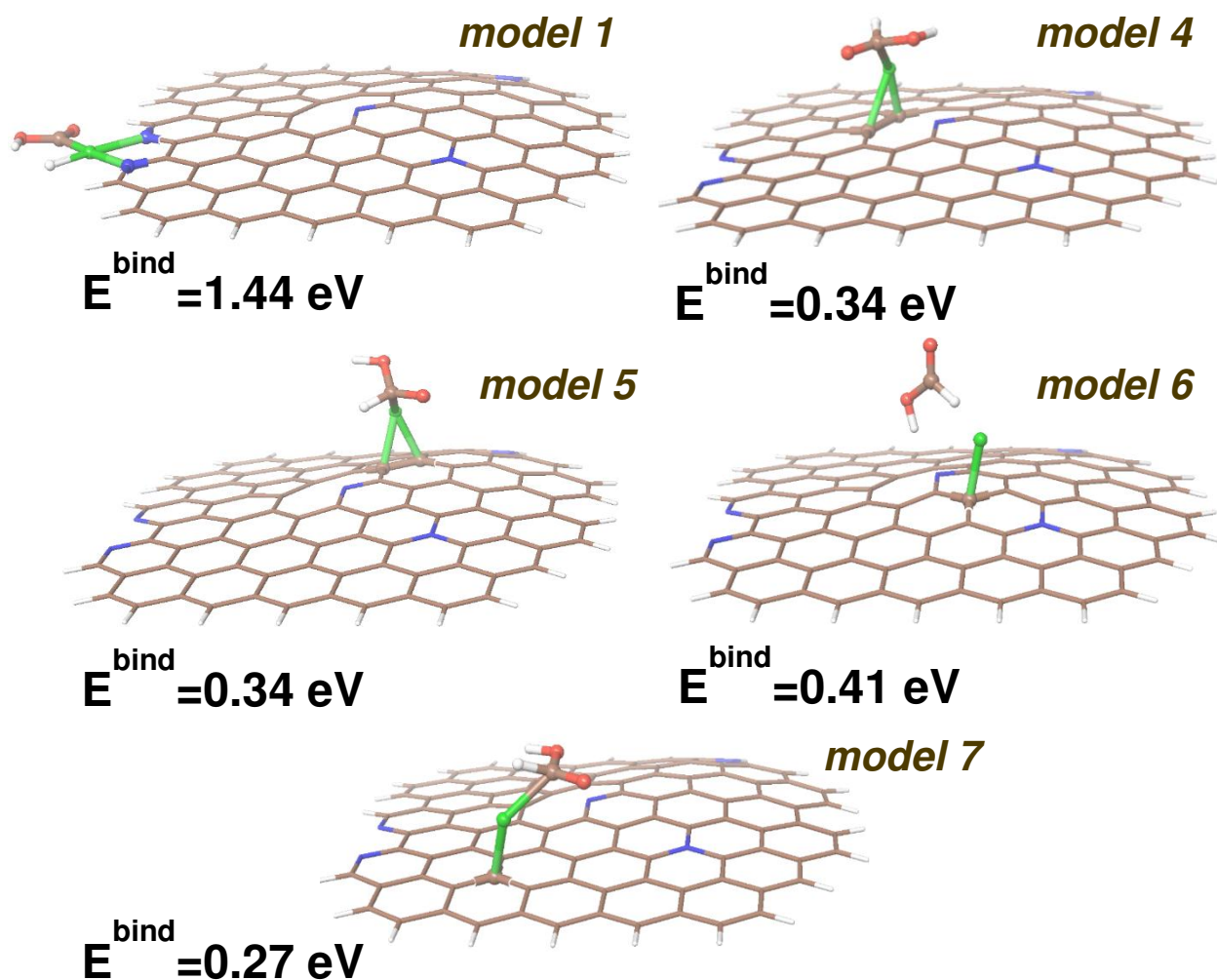
model 1

E^{bind}=1.44 eV

model 4

E^{bind}=0.34 eV

model 5

E^{bind}=0.34 eV

model 6

E^{bind}=0.41 eV

model 7

E^{bind}=0.27 eV

Figure 9. Geometries of models with formic acid molecule over Pd atoms located in different positions of nitrogen-containing graphene fragment optimized at PBE/LACVP*+ level and corresponding binding energies. Blue colour indicates N, red – O, brown – C, green – Pd, light-gray – H.

optimized structure, Pd is linked with H atom and C atom of carboxyl fragment. These atoms were previously covalently bonded in the formic acid molecule. Since the calculation was done at 0 K, the reconstructions occur without an energy barrier. We found from the calculation results two critical points for the C-H bond rupture in the formic acid molecule. The structures

corresponding to these points together with those of starting point and final one are shown in Figure 10. The formic acid is oriented to the Pd atom by the H(C) fragment (step 1), the
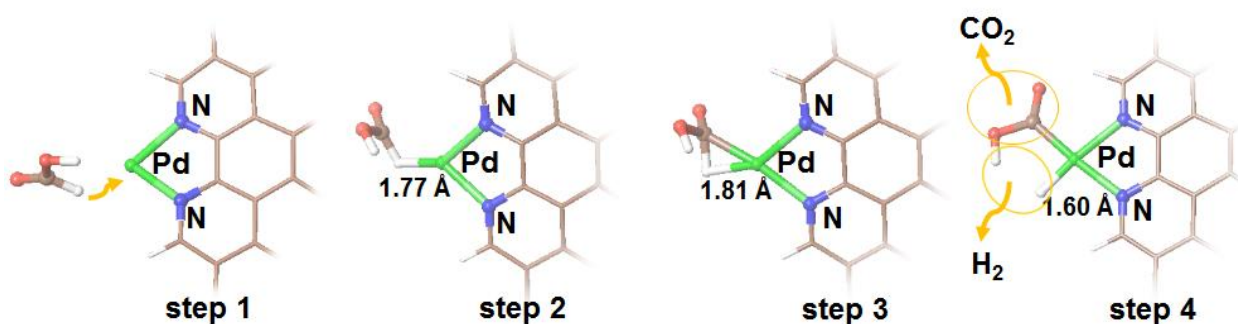

Figure 10. Consequence of reaction steps for the formic acid interaction with an isolated Pd atom stabilized by two pyridinic nitrogen atoms on the edge of graphene fragment (red – oxygen, brown carbon, light-gray – hydrogen). The numbers show the Pd-H distances in complexes formed in steps 2–4.

molecule is approaching up to a distance of 1.77 Å (step 2), the molecule is reoriented so that Pd forms the bonds with carbon (2.08 Å) and hydrogen (1.81 Å) (step 3). Such interaction causes an elongation of the H-C bond from 1.18 Å to 1.26 Å. This bond breaks and Pd forms covalent bonds with C and H in the final configuration (Table S4, Supporting information). Note, that in the final configuration the hydrogen atom in the OH fragment of formic acid is located closely to the hydrogen atom attached to the Pd atom (the distance is 1.89 Å), that at elevated temperatures could help in the formation of H_2 molecule. Hence, the final state of the geometry optimization (structure in step 4) might be considered as a transition complex for the H_2 and CO_2 evolution.

Summarizing the main results of the theoretical part of the work, the structure of the active site involving a Pd atom attached to a couple of edged pyridinic nitrogen atoms is the most energetically favorable as compared to other considered structures. This active site interacts

26

strongly with formic acid leading to the rupture of the C–H bond and the formation of chemisorbed hydrogen atom and carboxyl fragment.

3.6. Single-site catalysis with Pd for formic acid decomposition. As we reported above, single isolated Pd atoms supported mainly on oxide supports were shown to be active in reactions of oxidation[13-15] and CO_2 reduction.[16] However, for some of these reactions a deactivation of the catalyst was observed.[15] The studies of single-site catalysis are expanding[8,12-16,40-42] with the development of TEM equipment allowing imaging of isolated atoms existing often on the catalyst support together with metal clusters. Very recently, Arrigo et al.[27] came to a conclusion that Pd^{2+} species on N-doped carbon nanotubes were inactive in CO oxidation and hydrogenation of phenyl acetylene, but active in the electrochemical oxygen reduction reaction. Zhao et al.[43] showed that immobilized Pd^{2+} complexes attached to silica supports via sulfur atoms are active in liquid phase hydrogen production from HCOOH/NaHCOO mixtures at temperatures lower than 373 K.

Our experimental studies led to some important results. A significant difference in the TOF values (up to 3 times) was obtained for the catalysts based on the N-doped catalysts as compared to the N-free ones. This was in line with our earlier studies of the Ru^{25} and Pt^{24} catalysts with the same mean particle sizes for the N-free and N-doped samples and 1 wt.% loading of metal supported on carbon nanofibers. To explain the nitrogen-doping effect for the studied Pd catalysts we also have to take into account that the mean Pd particle sizes and Pd particle size distributions (Figure 2, Figure S3, Supporting information) for the N-doped and N-free Pd catalysts were very similar. We did not observe a difference in the shapes of nanoparticles in these samples. According to the XPS measurements, the electronic properties of the metal nanoparticles were also quite close (Figure 7b). Moreover, the ratio of the surface metal Pd concentration to the total concentration of Pd decreased with N-doping. Hence, the

significant increase of the catalytic activity of the N-functionalized catalyst cannot be assigned to the differences related to Pd nanoparticles observed by regular STEM.

Recently,[24,25] we proposed that activation of formic acid may take place on pyridinic nitrogen sites of the support with the formation of adduct/formate species and their further decomposition on metallic nanoparticles existing in the proximity to the formate species. However, the performed DFT studies have not supported this formate mechanism at least for the active site representing a single Pd atom attached to a couple of pyridinic nitrogen atoms. The reason can be that the formation of nitrogen-palladium bonds decreases substantially the basicity of the nitrogen atoms and their ability to activate formic acid. In agreement, we showed that a Pd atom attachment causes a reduction of the electron density over these nitrogen atoms (Figure S6, Supporting information).

The existence of isolated Pd^{2+} cations in our samples interacting with pyridinic nitrogen of the support clearly follows from aberration-corrected STEM, NEXAFS and XPS studies. Our DFT studies showed that the single isolated Pd atoms are the active sites for hydrogen production from formic acid, but only if they are coordinated by a couple of pyridinic nitrogen atoms on the edge of graphene sheet. In this case, the formic acid molecule dissociates on the Pd species into adsorbed hydrogen atom and carboxyl fragment. This was in line with some DFT studies[44,45] of the formic acid interaction with Pd facets, showing that the dehydrogenation possesses a lower energy barrier if it takes place via the path involving carboxyl species as compared to the path via formate species. However, alternative results, where the decomposition takes place via formate species were obtained by other groups.[46,47] Feng et al.[37] performed some DFT calculations of the interaction of the formic acid molecule with a Pt atom located on N-doped carbon nanotubes, but did not consider a Pt atom on nitrogen sites located on the edge of the carbon nanotubes, which can provide much stronger interaction accompanied by dissociation of the molecule.

The formation of the Pd species attached to a couple of pyridinic nitrogen sites is also in line with the ability of palladium to form chelate complexes with N-containing organic ligands, for example, with phenanthroline containing a couple of pyridinic type nitrogen atoms. The structure of some complexes of Pd with this ligand is well studied.[48-50] These complexes were used as homogeneous catalysts for different reactions. Thus, recently it was shown that complexes of some noble metals[51] and iron[52] with phenanthroline type ligands are active in conversion of CO_2 to formate species[51] and in dehydrogenation of formic acid.[52] Generally, the activity of homogeneous catalysts based on metal complexes is higher in formic acid dehydrogenation than that of heterogeneous catalysts containing metal nanoparticles.[2,33] Hence, the present research with N-functionalized carbon covers a gap between homogeneous and heterogeneous catalysis in this field discovering active isolated Pd^{2+} cations stable at least up to 573 K in hydrogen. The obtained Pd sites attached to a couple of pyridinic nitrogen atoms on the edge of graphene sheet demonstrate also an excellent stability in the reaction conditions (Figure 4). This can be related to the strong interaction of Pd atoms with nitrogen atoms and high stability of the N-functionalized carbon participating in the interaction with Pd as a ligand as compared to the ligands traditionally used in metal complexes for homogeneous catalysis.

4. CONCLUSIONS

Pd supported on nitrogen-functionalized mesoporous carbon support has demonstrated 3 times higher catalytic activity (TOFs) in formic acid dehydrogenation as compared to the activity of Pd supported on nitrogen-free carbon in spite of close mean metal particle size and particle size distributions determined from regular TEM studies. This was assigned to the activity of isolated Pd^{2+} cations stabilized by a couple of pyridinic type nitrogen atoms located on the edge of graphene sheet. The presence of such species was confirmed by aberration-corrected STEM, NEXAFS and XPS combined with DFT calculations. The DFT calculations demonstrated the

reactivity of these Pd species with respect to formic acid showing the decomposition of the formic acid molecule into adsorbed hydrogen atom and carboxyl fragment. Hence, we show for the first time single-site catalysis for the hydrogen production from formic acid decomposition with Pd atoms supported on N-doped carbon. The used materials demonstrated an excellent stability in the conditions of the reaction at least within 30 h. A further research in the area of single-site heterogeneous catalysis for conversion of biomass derived chemicals to useful products may lead to the creation of novel active, selective and stable catalysts.

ASSOCIATED CONTENT

Supporting Information

Chemical composition of carbon supports (Table S1), relative content of nitrogen forms (Table S2), comparison of experimental and theoretical binding energies for N 1s (Table S3), distances between the formic acid molecule and a Pd atom (Table S4), nitrogen sorption isotherms and pore size distributions (Figure S1), HAADF/STEM images of the catalysts (Figures S2 and S4), comparison of the particle size distributions for the N-free and N-doped Pd samples (Figure S3), models of the attachment of a Pd atom to N-doped graphene (Figure S5) and electron density surfaces for N-containing graphene with and without Pd (Figure S6). This material is available free of charge via the Internet at http://pubs.acs.org.

AUTHOR INFORMATION

Corresponding Authors

*E-mail: dmitri.bulushev@catalysis.ru, bul@niic.nsc.ru

Notes

The authors declare no competing financial interest.

REFERENCES

(1)   Grasemann, M.; Laurenczy, G. *Energy Environ. Sci.* **2012**, *5*, 8171-8181.

(2)   Loges, B.; Boddien, A.; Gartner, F.; Junge, H.; Beller, M. *Top. Catal.* **2010**, *53*, 902-914.

(3)   Bulushev, D. A.; Ross, J. R. H. *Catal. Today* **2011**, *163*, 42-46.

(4)   Heeres, H.; Handana, R.; Chunai, D.; Rasrendra, C. B.; Girisuta, B.; Heeres, H. J. *Green Chem.* **2009**, *11*, 1247-1255.

(5)   Serrano-Ruiz, J. C.; Braden, D. J.; West, R. M.; Dumesic, J. A. *Appl. Catal., B* **2010**, *100*, 184-189.

(6)   Hayes, D. J.; Fitzpatrick, S.; Hayes, M. H. B.; Ross, J. R. H. In *Biorefineries-Industrial Processes and Products*; Kamm, B., Gruber, P. R., Kamm, M., Eds.; Wiley-VCH: Weinheim, 2006; Vol. 1, p 139-164.

(7)   Li, J.; Ding, D. J.; Deng, L.; Guo, Q. X.; Fu, Y. *ChemSusChem* **2012**, *5*, 1313-1318.

(8)   Yi, N.; Saltsburg, H.; Flytzani-Stephanopoulos, M. *ChemSusChem* **2013**, *6*, 816-819.

(9)   Ciftci, A.; Ligthart, D.; Pastorino, P.; Hensen, E. J. M. *Appl. Catal. B* **2013**, *130*, 325-335.

(10)   Bi, Q. Y.; Du, X. L.; Liu, Y. M.; Cao, Y.; He, H. Y.; Fan, K. N. *J. Am. Chem. Soc.* **2012**, *134*, 8926-8933.

(11)   Ojeda, M.; Iglesia, E. *Angew. Chem., Int. Ed.* **2009**, *48*, 4800-4803.

(12)   Flytzani-Stephanopoulos, M. *Acc. Chem. Res.* **2014**, *47*, 783-792.

(13)   Abbet, S.; Heiz, U.; Hakkinen, H.; Landman, U. *Phys. Rev. Lett.* **2001**, *86*, 5950-5953.

(14)   Hackett, S. E. J.; Brydson, R. M.; Gass, M. H.; Harvey, I.; Newman, A. D.; Wilson, K.; Lee, A. F. *Angew. Chem., Int. Ed.* **2007**, *46*, 8593-8596.

(15)   Peterson, E. J.; DeLaRiva, A. T.; Lin, S.; Johnson, R. S.; Guo, H.; Miller, J. T.; Kwak, J. H.; Peden, C. H. F.; Kiefer, B.; Allard, L. F.; Ribeiro, F. H.; Datye, A. K. *Nat. Commun.* **2014**, *5*, 4885.

(16)   Kwak, J. H.; Kovarik, L.; Szanyi, J. *ACS Catal.* **2013**, *3*, 2094-2100.

(17)   Bulushev, D. A.; Beloshapkin, S.; Ross, J. R. H. *Catal. Today* **2010**, *154*, 7-12.

(18)   Bulushev, D. A.; Jia, L. J.; Beloshapkin, S.; Ross, J. R. H. *Chem. Commun.* **2012**, *48*, 4184-4186.

(19)   O'Neill, B. J.; Gürbüz, E. I.; Dumesic, J. A. *J. Catal.* **2012**, *290*, 193-201.

(20)   Tedsree, K.; Li, T.; Jones, S.; Chan, C. W. A.; Yu, K. M. K.; Bagot, P. A. J.; Marquis, E. A.; Smith, G. D. W.; Tsang, S. C. E. *Nat. Nano* **2011**, *6*, 302-307.

(21) Wang, Z.-L.; Yan, J.-M.; Ping, Y.; Wang, H.-L.; Zheng, W.-T.; Jiang, Q. *Angew. Chem., Int. Ed.* **2013**, *52*, 4406-4409.

(22) Bulushev, D. A.; Beloshapkin, S.; Plyusnin, P. E.; Shubin, Y. V.; Bukhtiyarov, V. I.; Korenev, S. V.; Ross, J. R. H. *J. Catal.* **2013**, *299*, 171-180.

(23) Bulushev, D. A.; Bulusheva, L. G.; Beloshapkin, S.; O'Connor, T.; Okotrub, A. V.; Ryan, K. M. *ACS Appl. Mater. Interfaces* **2015**, *7*, 8719-8726.

(24) Jia, L. J.; Bulushev, D. A.; Podyacheva, O. Y.; Boronin, A. I.; Kibis, L. S.; Gerasimov, E. Y.; Beloshapkin, S.; Seryak, I. A.; Ismagilov, Z. R.; Ross, J. R. H. *J. Catal.* **2013**, *307*, 94-102.

(25) Zacharska, M.; Podyacheva, O. Y.; Kibis, L. S.; Boronin, A. I.; Senkovskiy, B. V.; Gerasimov, E. Y.; Taran, O. P.; Ayusheev, A. B.; Parmon, V. N.; Leahy, J. J.; Bulushev, D. A. *ChemCatChem* **2015**, *7*, 2910-2917.

(26) Podyacheva, O. Y.; Ismagilov, Z. R. *Catal. Today* **2015**, *249*, 12-22.

(27) Arrigo, R.; Schuster, M. E.; Xie, Z.; Yi, Y.; Wowsnick, G.; Sun, L. L.; Hermann, K. E.; Friedrich, M.; Kast, P.; Havecker, M.; Knop-Gericke, A.; Schlogl, R. *ACS Catalysis* **2015**, *5*, 2740-2753.

(28) Arrigo, R.; Schuster, M. E.; Abate, S.; Wrabetz, S.; Amakawa, K.; Teschner, D.; Freni, M.; Centi, G.; Perathoner, S.; Havecker, M.; Schlogl, R. *ChemSusChem* **2014**, *7*, 179-194.

(29) Stonkus, O. A.; Kibis, L. S.; Podyacheva, O. Y.; Slavinskaya, E. M.; Zaikovskii, V. I.; Hassan, A. H.; Hampel, S.; Leonhardt, A.; Ismagilov, Z. R.; Noskov, A. S.; Boronin, A. I. *ChemCatChem* **2014**, *6*, 2115-2128.

(30) Shlyakhova, E. V.; Bulusheva, L. G.; Kanygin, M. A.; Plyusnin, P. E.; Kovalenko, K. A.; Senkovskiy, B. V.; Okotrub, A. V. *Phys. Status Solidi B* **2014**, *251*, 2607-2612.

(31) Perdew, J. P.; Burke, K.; Ernzerhof, M. *Phys. Rev. Lett.* **1996**, *77*, 3865.

(32) Kondrat, S. A.; Shaw, G.; Freakley, S. J.; He, Q.; Hampton, J.; Edwards, J. K.; Miedziak, P. J.; Davies, T. E.; Carley, A. F.; Taylor, S. H.; Kielyb, K. J.; Hutchings, J. J. *Chem. Sci.* **2012**, *3*, 2965-2971.

(33)   Jia, L.; Bulushev, D. A.; Beloshapkin, S.; Ross, J. R. H. *Appl. Catal., B* **2014**, *160-161*, 35-43.

(34)   Bulusheva, L. G.; Okotrub, A. V.; Fedoseeva, Y. I.; Kurenya, A. G.; Asanov, I. P.; Vilkov, O. Y.; Koos, A. A.; Grobert, N. *Phys. Chem. Chem. Phys.* **2015**, *17*, 23741-23747.

(35)   Artyushkova, K.; Kiefer, B.; Halevi, B.; Knop-Gericke, A.; Schlogl, R.; Atanassov, P. *Chem. Commun.* **2013**, *49*, 2539-2541.

(36)   Mananghaya, M.; Rodulfo, E.; Santos, G. N.; Villagracia, A. R.; Ladines, A. N. *J. Nanmater.* **2012**, *2012*, 104891.

(37)   Feng, H.; Ma, J.; Hu, Z. *J. Mater. Chem.* **2010**, *20*, 1702-1708.

(38)   Li, Y. H.; Hung, T. H.; Chen, C. W. *Carbon* **2009**, *47*, 850-855.

(39)   Tang, Y. N.; Yang, Z. X.; Dai, X. Q. *J. Chem. Phys.* **2011**, *135*, 224704.

(40)   Flytzani-Stephanopoulos, M.; Gates, B. C. *Annu. Rev. Chem. Biomolec. Eng.* **2012**, *3*, 545-574.

(41)   Bradley, S. A.; Sinkler, W.; Blom, D. A.; Bigelow, W.; Voyles, P. M.; Allard, L. F. *Catal. Lett.* **2012**, *142*, 176-182.

(42)   Yang, X. F.; Wang, A. Q.; Qiao, B. T.; Li, J.; Liu, J. Y.; Zhang, T. *Acc. Chem. Res.* **2013**, *46*, 1740-1748.

(43)   Zhao, Y.; Deng, L.; Tang, S. Y.; Lai, D. M.; Liao, B.; Fu, Y.; Guo, Q. X. *Energy Fuels* **2011**, *25*, 3693-3697.

(44)   Herron, J. A.; Scaranto, J.; Ferrin, P.; Mavrikakis, M. *ACS Catal.* **2014**, *4*, 4434-4445.

(45)   Yoo, J. S.; Abild-Pedersen, F.; Norskov, J. K.; Studt, F. *ACS Catal.* **2014**, *4*, 1226-1233.

(46)   Hu, C. Q.; Ting, S. W.; Chan, K. Y.; Huang, W. *Int. J. Hydrogen Energy* **2012**, *37*, 15956-15965.

(47)   Luo, Q.; Feng, G.; Beller, M.; Jiao, H. *J. Phys. Chem. C* **2012**, *116*, 4149-4156.

(48)   Demidov, V. N.; Simanova, S. A.; Savinova, A. I.; Zinchenko, A. V.; Pakhomova, T. B.; Aleksandrova, E. A. *J. Struct. Chem.* **2010**, *51*, 296-302.

(49)   Stoyanov, E. S.; Chesalov, Y. A.; Kochubey, D. I.; Stolyarov, I. P.; Vargaftik, M. N. *J. Struct. Chem.* **2003**, *44*, 376-380.

(50)   Calligaris, M.; Zangrando, E.; Milani, B.; Marson, A. *Eur. J. Inorg. Chem.* **2005**, *4*, 704-712.

(51)   Himeda, Y. *Eur. J. Inorg. Chem.* **2007**, 3927-3941.

(52)   Boddien, A.; Loges, B.; Gartner, F.; Torborg, C.; Fumino, K.; Junge, H.; Ludwig, R.; Beller, M. *J. Am. Chem. Soc.* **2010**, *132*, 8924-8934.